Instrument Science Report ACS 2024-06

Implementing an Ubercal Model for ACS/WFC

R. E. Ryan Jr., A. Bellini, Y. Cohen
September 26, 2024

Abstract

We implement an Ubercal model for the photometric repeatability for the Advanced Camera for Surveys, Wide-Field Channel for the F606W filter based on observations of 47 Tuc for post SM4. We have identified and measured 31 523 *unique stars from* 422 *independent exposures using the* `hst1pass` *photometric toolkit, so each star has on average* 59.3 *measurements. Since these stars fall on distinct pixels (often in different chips), this dataset represents a unique opportunity to improve the relative photometric calibration. Specifically, we implement a sixth-order polynomial form for the low-frequency flat for each detector separately, time-dependent sensitivity losses for each amplifier, and a systematic uncertainty floor. Additionally, we find evidence that very short exposures* ($\lesssim 200$ *s) have a small bias in their photometry of 0.08 mmag/s, although the physical explanation of this is unclear. Further, we find that the sensitivity of the four amplifiers is degrading with time at a rate of* $\sim 1.5-2.0$ *mmag/yr depending on the amplifier. Similarly, we find that WFC2 sensitivity is depressed by* ~ 0.05 *mag with respect to WFC1. Finally, we see that the photometric scatter is still larger than expected, implying there are systematic effects still unaddressed, and we find strong evidence for serial CTE losses. Future work may consider other filters (such as F814W), linking to more fields (such as the deep fields), or including other systematic terms (such as characterizing the serial CTE).*

1 Introduction

It is impossible to overstate the importance of accurate and precise calibrations, as they affect every scientific study. Therefore, it is common to separate *relative* from *absolute* calibrations (*e.g.* Padmanabhan et al. 2008), as the former can be achieved to a high degree with science observations, dedicated hardware, or specialized observations (*e.g.* internal or dome flat fields, astrometric standard fields). Indeed, the Wide-Field Instrument on the forthcoming *Nancy Grace Roman Space Telescope* has a Relative Calibration System (RCS; Deustua, Rubin, Hounsell et al. 2021) to minimize all sources of relative photometric systematics. In contrast, absolute calibration requires standard observations that have been meticulously monitored, which can be challenging given the source brightness, required telescope time, and sky coverage (*e.g.* Deustua, Kent, & Smith 2013). For these reasons, this report is aimed at characterizing various systematic terms that may affect the relative photometric calibration for the *Advanced Camera for Surveys* (ACS) on the *Hubble Space Telescope* (HST).

Relative calibration can be made to address a vast class of effects (*e.g.* spatial or temporal effects). A significant term in the spatial component of the relative calibration budget comes from the *flat field* (an observation that describes the relative differences in the interpixel sensitivity), which is often determined by illuminating the detector with a flat light source. While this light source may come from a variety of sources (*e.g.* the night sky or a screen mounted in the dome), for the ACS/WFC it was measured in the laboratory with the Refractive Aberrated Simulator/Hubble Opto-Mechanical Simulator (RAS/HOMS) with a continuum light source. Additionally, the interpixel sensitivity will vary with wavelength so a flat-field must be obtained separately for each band. However, the differences in the shape of the spectrum of the illuminating source (over the wavelengths in the bandpass) and that of the typical astrophysical source will lead to discrepancies in the calibrated flux of said source.

Shortly after ACS was installed on HST, it was shown that the flux of standard stars and stellar fields showed photometric residuals on large spatial scales (*e.g.* Van der Marel 2003). This variance represents a systematic uncertainty floor that will limit the signal-to-noise of any photometric observation, regardless of the observing parameters (*e.g.* exposure time, dithers, source brightness, *etc.*). This systematic is typically addressed using a low-frequency flat (hereafter, *L-flat*) that is constructed to minimize the scatter of repeated observations (*e.g.* Mack et al. 2002; Van der Marel 2003; Cohen, Grogin, & Bellini 2020).

The method of comparing repeated observations of some sources to understand systematic uncertainties has been successful with other observatories. For example, Padmanabhan et al. (2008) implemented a scheme (hereafter, Ubercal) for the Sloan Digital Sky Survey (SDSS) that encapsulated all of the (known) effects into a single model that minimized the aggregate photometric scatter. Since SDSS is a ground-based, drift-scan survey, there are several effects that are not relevant here (*e.g.* airmass, photometricity) or are framed differently than our needs (*e.g.* a one-dimensional flat field). Based on this, Padmanabhan et al. (2008) was able to reduce the photometric scatter to $\lesssim$1%. Later, Wittman, Ryan, & Thorman (2012) adapted the UberCal methodology to the Deep Lens Survey (DLS), a classic "shift-and-stare" survey, which reduced the photometric residuals from $\sim$13% to $\lesssim$1%. The common theme between these examples is a complete characterization of all systematic effects in the photometry.

Importantly, linking repeated observations to determine a correction to the flat field necessarily implies linking data over some temporal scale, which introduces additional complications. For example, if the sensitivity of the instrument (or detector) varies with time (*e.g.* Bohlin, Ryon, & Anderson 2020), then these effects must be incorporated. With these ideas in mind, this report aims to develop an Ubercal method that encapsulates multiple relative calibration components (including the L-flat) for the ACS/WFC.

This report is organized as follows: § 2 describes the archival observations of 47 Tuc, § 3 defines the photometric model for ACS/WFC, § 4 presents simulated data used to validate our methods, § 5 catalogs our results, and § 6 gives some concluding remarks with thoughts for future work.

2 Observations, Data Reduction, and Photometry

We analyze 422 exposures of 47 Tuc in the F606W filter with ACS/WFC from 2009 to 2023, collected either as GO or calibration observations, and list all the program IDs in Appendix A. The data subtend $\sim$42 arcmin^2 that is $\sim$7 arcmin from the cluster center. We reduce these observations using version 10.3.5 of CALACS, but set the `PFLTFILE=m2f1516ej_pfl.fits`. It is important to note, this flat field is a largely a choice and all subsequent spatial corrections are with respect to this file. We use the current version of the pixel-based charge-transfer efficiency (CTE; Anderson 2022a).

We employ `hst1pass` (Anderson 2022b) to both find and measure the relatively bright and isolated stars in each exposure through point-spread-function (PSF) fitting based on the suite of effective PSF models that span a range of focus levels (Bellini et al. 2018). We additionally perturbed these PSF models in each exposure to account for telescope breathing. We correct the stellar positions in each catalog for geometric distortion using the models by (Anderson & King 2006).

The effective pixel area changes over the field-of-view due to the image distortion, which is also known to change with time (*e.g.* Úbeda & Kozhurina-Platais 2013; Borncamp et al. 2015; Kozhurina-Platais et al. 2015; Hoffmann & Kozhurina-Platais 2020). To account for this, we manually apply the pixel-area correction to the `hst1pass` catalogs using the time-dependent distortion present in the `SCI`-extension headers using `stwcs.updatewcs.updatewcs()`. Now, the relative pixel area is the Jacobian of the distortion model, which is described by Simple-Imaging Polynomials (SIP).

We constructed a reference coordinate system based on Gaia DR3 (Gaia Collaboration et al. 2016, 2023) data with North-up/East-left, a pixel scale of exactly $0\farcs050$ pix^{-1}, and the center of the field at pixel position $(x, y) = (5000, 5000)$ pix. We used general six-parameter linear transformations to map each measured star in each catalog on to the reference system, initially using the few unsaturated HST stars in common with the Gaia catalog, and then refined only using well-measured HST stars. Multiple measurements of the same stars in the reference system are then averaged together in both position and magnitude into a master frame catalog, which contains 66 306 stars measured in at least 3 individual exposures.

In what follows, we will use the word "fluence" to refer to the total number of astrophysical photoelectrons recorded in a pixel (or aperture) after the standard CCD processing is completed (*e.g.* bias, dark, flat-field, *etc.*) and refer to this as F, which is in units of e^-. We will refer to "flux" as the rate at which the same astrophysical photoelectrons are measured and denote it as f, and the units will be e^-/s unless explicitly stated as otherwise (such as applying the absolute calibrations). To determine an uncertainty for each photometric measurement, we assume the statistics are dominated by the Poissonian noise from the source and the sky background, hence the uncertainty on the magnitude is:

$$\delta m = \left(\frac{2.5}{\ln 10}\right) \frac{\sqrt{F + B}}{F}. \tag{1}$$

where B is the fluence from the local sky to each star, measured just outside the PSF fitting radius. Importantly, these estimates are used to set weights in the optimization process (to be discussed in more detail below), but will be updated to account for systematic uncertainties.

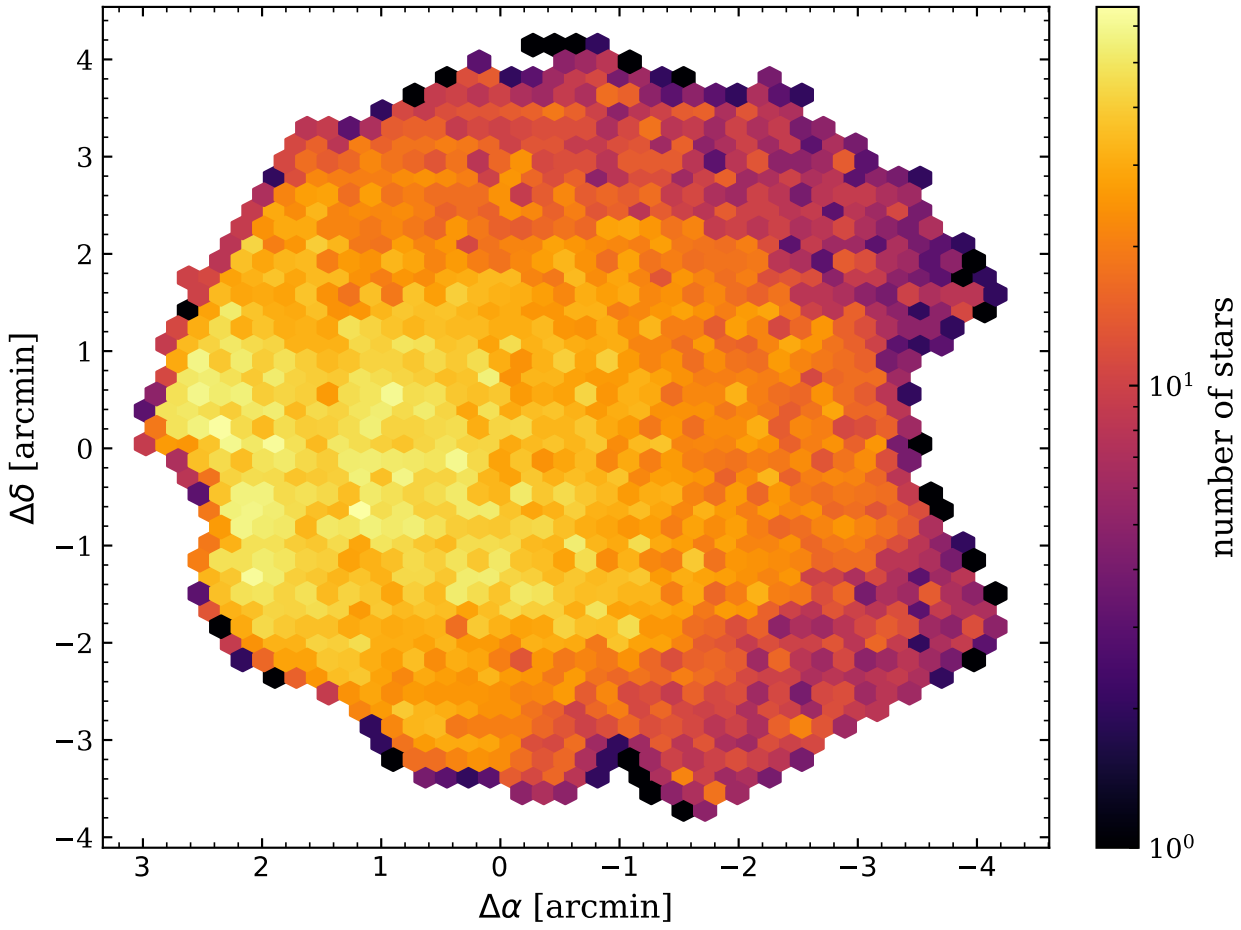

Figure 1: The spatial distribution of the 31 523 stars from the joined catalog of all measurements that satisfy our selection criteria. The center of 47 Tuc is $\sim 7'$ to the left. It is important to note, many of these stars are rejected for the final analysis as discussed in § 2.

From this analysis, we find there are 66 306 stars with 6 449 062 independent measurements, however for our analysis, it is more important to restrict the size of the sample to only clean/reliable measurements than to increase the sample size. Therefore, we apply these selection criteria to our catalogs:

1. high fluence: $F \geq 10^4$ e^-;
2. reliable PSF fit and avoiding saturated stars: $0 < Q \leq 0.15$;
3. sharp PSF model: $|C| < 0.03$;
4. positive background fluence (more below): $B > 0$ e^-;
5. remove sources associated with the donut that is likely associated with differences in chip thickness on WFC2 (*e.g.* Krist 2003): $(x - 2116)^2 + (y - 1468)^2 \geq 230^2$.

Our fluence criterion implies that the selected stars have a minimum signal-to-noise of 100. See Anderson (2022b) for a description of the quality of fit Q and the sharpness-like C parameters. This results in a catalog of 31 523 stars with 1 868 996 independent measurements, and we show their spatial distribution in Figure 1.

As mentioned above, there are $N_{\rm exp} = 422$ independent exposures, each having a unique pointing $(\alpha_j, \delta_j, \varpi_j)$[1], exposure time (t_j), and date of observation (T_j), and consequently a unique number of stars $(N^\star_j)$ — where j is an "exposure index". However, cluster stars have measured positions $(x_{i,j}, y_{i,j})$ on particular detectors[2] $(c_{i,j})$ and instrumental fluxes $(f_{i,j})$ — where i is the "source index". There are $N_{\rm meas} = \sum_i N^\star_i = 1\,868\,996$ distinct stellar measurements derived from $N^\star = 31\,523$ separate stars, hence we have on average $\rho = 59.3$ measurements per star and every star has at least 3 measurements. Using these data, we adopt the analysis philosophy of Padmanabhan et al. (2008), and parameterize all of the (known) systematic effects.

3 The Ubercal Model

In the most basic terms, an Ubercal model describes perturbations that are applied to a collection of measurements that minimize the scatter for repeated measurements. In this case, we are considering measurements of photometric magnitude, althought it is straightforward to generalize the model formulation to consider any measurement (such as a grism spectral dispersion). Therefore we are to determine additive magnitude offsets to minimize the scatter in the photometry of each object. To be clear, we are framing the problem in "magnitude-space" (*e.g.* Van der Marel 2003; Padmanabhan et al. 2008; Wittman, Ryan, & Thorman 2012) so that perturbations enter as additive terms (in many cases they are even linear terms). While this formulation simplifies the solution process, it complicates the uncertainty propagation. As described in Section 2, we are only considering stars with very high signal-to-noise, which mitigates this concern. On the other hand, the analogous model in "flux-space" (*e.g.* Cohen, Grogin, & Bellini 2020) implements multiplicative corrections, which breaks much of the linearity.

[1] These coordinates refer to R.A., Dec., and position angle, respectively.
[2] ACS/WFC has two detectors, therefore $c \in \{1, 2\}$.

3.1 Physical Effects

3.1.1 L-Flat Corrections

As alluded to in Section 1, the L-flat is a multiplicative correction to the pixel-to-pixel flat (hereafter, P-flat). As done in Van der Marel (2003); Cohen, Grogin, & Bellini (2020), we describe the spatial dependence of the L-flat as an expansion in orthonormal basis functions. We adopt the Legendre basis for direct comparisons to previous work, but more importantly, their orthonormality condition further simplifies the problem. Since the Legendre polynomials are defined on the domain $[-1, 1]$, we must remap the (x, y) coordinates of a source according to:

$$x' = 2\,(x/n_x) - 1 \tag{2}$$
$$y' = 2\,(y/n_y) - 1, \tag{3}$$

where $(n_x, n_y) = (4096, 2048)$ are the dimensions of the detector. Further, to avoid degeneracies between the flat-field normalization and the absolute flux calibration (*e.g.* Padmanabhan et al. 2008), we require the L-flat have no net power, which implies the average over the detector should be zero. This is trivially enforced by requiring the first term in the Legendre expansion to be exactly zero, since the zeroth polynomial is $P_0(x) = 1$. Therefore, the complete expansion for the L-flat as a Legendre series of order Z is:

$$\mathcal{L}_c(x, y) = \sum_{k,l}^{Z} \alpha_{c,k,l}\, P_k(x')\, P_l(y') \tag{4}$$

where the summation extends over all combinations of k and l such that $1 \leq k + l \leq Z$, where (k, l) represent the individual basis orders and Z is the combined order. By construction, this flat-field expansion will have $Z(Z+3)/2$ free parameters per chip, which are given as the $\{\alpha\}$. As an aside, any other orthonormal polynomial representation (*e.g.* Chebyshev) will give exactly the same result albeit with different (but equivalent) coefficients due to their different orthogonality conditions, which may cause the zeroth term of the expansion to be non-zero.

3.1.2 Time-Dependent Sensitivity

It is well known that CCDs lose sensitivity over time (*e.g.* Bohlin, Ryon, & Anderson 2020), therefore we must encapsulate this effect when comparing photometry over many years. We do this by introducing a "time-dependent sensitivity" (TDS) that is normalized to unity at a fiducial time and decays for all subsequent times. To emulate the findings of Bohlin, Ryon, & Anderson (2020), we adopt a linear-decline in magnitude of the form:

$$\mathcal{S}_a(T) = \beta_a(T - T_0) + \gamma_a, \tag{5}$$

where a refers to the amplifiers[3] and $T_0 = 2009$ is our adopted zeropoint in time. Currently, we do not consider data prior to Servicing Mission 4 (SM4), therefore we have no observing

[3] ACS/WFC has four amplifiers, therefore $a \in \{A, B, C, D\}$.

dates with $T<2009$. Although we expect the amplifiers to qualitatively degrade in a similar fashion, there are no assurances this is quantitatively true. Therefore each amplifier has a unique decay constant (in units of mag/yr); and these constants $\{\beta\}$ are unknowns to be determined below. Importantly, to avoid a similar degeneracy in Section 3.1.1, we must fix one of the offsets $\gamma_A=0$ mag. Additionally, this representation allows the four amplifiers to modulate independently, but when taken in pairs on the same detector (*e.g.* A/B and C/D), then this will emulate the two-chip solutions that were implemented for *Wide-Field Camera 3* UVIS detector (*e.g.* Mack 2016).

3.1.3 Systematic Uncertainty

The photometric uncertainties described in Section 2 only account for Poisson shot noise, and not any systematic uncertainty. To address this, we introduce a systematic noise term that scales with the corrected flux, and so the combined uncertainty is:

$$\sigma = \sqrt{\delta m^2 + e^{2\eta}\,\tilde{m}^2} \tag{6}$$

where $\tilde{m}$ is the corrected magnitude (more on this below). The parameter η modulates the systematic uncertainty and is determined in the optimization process.

3.2 Model Solution

Now the correction to the photometry is given by a sum of the above physical components:

$$\Delta m_{a,c}(x, y, T) = \mathcal{L}_c(x, y) + \mathcal{S}_a(T), \tag{7}$$

where each of the observed properties (x, y, T, a, c) should have subscripts indicating the jth measurement of the ith star, but they are omitted for ease of notation. We will further simplify the notation and refer to these corrections as $\Delta m_{i,j}$. We seek the collection of unknowns: $\boldsymbol{\theta} = \{\boldsymbol{\alpha}, \boldsymbol{\beta}, \boldsymbol{\gamma}, \eta\}$ to minimize the scatter, which requires defining the "true" magnitude for the ith star ($\hat{m}_i$). With that, the corrected measurement is (by construction) given as: $\tilde{m}_{i,j} = m_{i,j} + \Delta m_{i,j}$. Now the goodness-of-fit metric must account for the usual uncertainty-weighted difference but also the variation associated with the systematic uncertainty:

$$\psi_i^2(\boldsymbol{\theta}) = \overbrace{\sum_{j=1}^{N_i} \left(\frac{\hat{m}_i - \tilde{m}_{i,j}}{\sigma_{i,j}} \right)^2}^{\chi_i^2(\boldsymbol{\theta})} + \overbrace{\sum_{j=1}^{N_i} \ln\left(2\pi\sigma_{i,j}^2\right)}^{\xi_i^2(\boldsymbol{\theta})}. \tag{8}$$

The first term represents the usual χ^2, while the second term $\xi_i^2(\boldsymbol{\theta})$ represents the normalization of the likelihood function and is often omitted as it rarely explicitly depends on $\boldsymbol{\theta}$. However, this is expressly not true for our model as η modulates the uncertainties (see equation (6)), and so it cannot be neglected. Now the total objective function is a sum over the stars: $\psi^2(\boldsymbol{\theta}) = \sum_i \psi_i^2(\boldsymbol{\theta})$, and the optimal vector of unknowns can be found by standard minimization techniques.

The problem of relative calibration via the Ubercal methodology has a very large parameter space; clearly the dimensionality of the $\boldsymbol{\theta}$ vector is relevant, but each of the true

magnitudes $\{\hat{m}\}$ are also free parameters. Hereafter, we will refer to these as *explicit* and *implicit* parameters (respectively), but critically there are $\sim 10^4$ unknowns, which is computationally challenging for standard optimization algorithms. To pare this down, we can solve for the implicit parameters given a choice of the model vector $\boldsymbol{\theta}$ by requiring $\chi^2(\boldsymbol{\theta})$ is minimized for $\{\hat{m}\}$. Since this minimum will occur when the gradient vanishes, we therefore require $\partial\chi^2(\boldsymbol{\theta})/\partial\hat{m}_i = 0$, which results in the constraint for the true magnitudes is:

$$\hat{m}_i(\boldsymbol{\theta}) = \frac{\sum_j w_{i,j}\,\tilde{m}_{i,j}(\boldsymbol{\theta})}{\sum_j w_{i,j}} \tag{9}$$

where the weights given as $w_{i,j} = \sigma_{i,j}^{-2}$. This shows that the optimal true magnitudes are the inverse-variance weighted average of the corrected magnitudes.

As mentioned above, the total number of unknowns is the number of parameters in $\boldsymbol{\theta}$ plus the number of unique stars: $N_{\boldsymbol{\theta}} + N^{\star}$, which we refer to as explicit and implicit parameters. Importantly, the number of knowns is just the total number of measurements: $N_{\rm meas} = 1\,868\,996$, which implies this is an over-constrained system. Therefore, we find the minimum of equation (8) using the L-BFGS-B algorithm in `scipy.optimize.minimize` (Virtanen et al. 2020). This method requires a function that returns the goodness-of-fit, which we compute by this simple procedure:

1. compute the magnitude corrections for some choice of $\boldsymbol{\theta}$ from equation (7);
2. compute the corrected magnitudes and updated uncertainties from equation (6);
3. compute the true magnitudes according to equation (9);
4. compute goodness-of-fit for each star separately from equation (8); and
5. return the total goodness-of-fit.

For the optimal model, we also return the true magnitudes and their inferred uncertainties to assess the quality of the final model.

4 Simulations

To validate our Ubercal model, we generate a series of simulated observations of 47 Tuc, but stress our goal here is to demonstrate the optimization techniques, and not necessarily establish any sort of systematic uncertainty on the results. As such, our simulations need only approximately match the true observations. Therefore we uniformly distributed 5000 stars over a field of 8096×8096 pix^2 (hereafter, the *metafield*), which is much larger than the coverage of the observations. These values are selected to ensure that each simulated image has a similar stellar surface density and average number of repeated measurements ~ 0.03 stars per arcsec^2. We do not try to simulate the spatial gradient in stellar density due to the cluster profile (see Figure 1). We assign each star a random apparent magnitude (in AB magnitudes) from a uniform distribution with $13 \leq m \leq 24$, which is roughly similar to that in the observations.

We create 200 random simulated exposures, each with a unique pointing and position angle, exposure time, date, and sky background from distributions of the observations. We assume the chip gap between the two detectors is exactly 50 pixels ($2\farcs5$), and maintain the relative positions of the two CCDs. We assume a random set of parameters for $\boldsymbol{\theta}$ and use these simulated catalogs of stars and fields to render noiseless fluences for each observation.

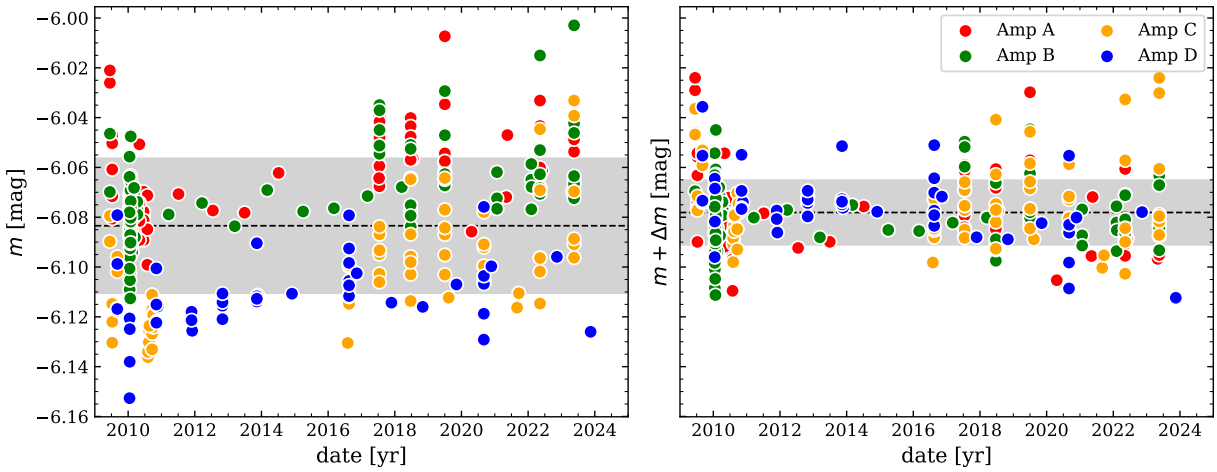

Figure 2: Lightcurves for star 14964. The left/right panels show the raw and the corrected lightcurve, respectively. The color of the plot symbols marks the amplifier on which the measurement was made, as indicated in the legend. The dotted line and the gray bar respectively illustrate the average and standard deviation. This highlights two effects: (1) the significant differences between the two detectors (the red/green versus the orange/blue points) and (2) the Ubercal model dramatically tightens the distribution from $\sigma_m = 27$ mmag to 13 mmag.

We draw a Poisson random number for each of these noiseless measurements, but must stress that the fluences are $\gtrsim 10^4$ e^- and so the differences between Poisson and Gaussian random variables is negligible. With these simulations, we were able recover the random input vector ($\boldsymbol{\theta}$) to $\lesssim 0.1\%$. As a final remark, we repeated this procedure for several random input vectors.

5 Results

We apply the above Ubercal to the 1 868 996 measurements of 31 523 stars from 47 Tuc with an L-flat with $Z = 6$ to find several results. In Figure 2, we show the lightcurve for star 14964 (which has the most measurements in our sample), with the amplifier for each measurement indicated by color. The left and right panels respectively show the native `hst1pass` photometry and that corrected by our Ubercal model. Two things are readily apparent by our results; firstly, the dispersion in the data dramatically decreases from $\sigma_m =$ 27 mmag to 13 mmag. But importantly, there is a significant difference between the two detectors, where the amplifiers A and B (red/green points) have a consistently different behavior than amplifiers C and D (orange/blue). This is reminiscent of the two-chip solution for WFC3/UVIS (Mack 2016).

Since the operating philosophy of Ubercal methods is to investigate all possible trends with variables, whether or not they are expected to be correlated (such as time), we consider additional residuals for other measurable quantities. In Figure 3, we show the corrected photometry as a function of the continuous variables: exposure time, sky surface brightness,

x- and y-coordinates. Surprisingly, there is a weak trend with exposure time (top left panel), where very short exposures ($t \lesssim 200$ s) show small systematic biases of order ~ 0.02 mag over this timescale. Although the root cause of this behavior is not obvious, it does not seem to be related to residual errors in the charge-transfer efficiency (CTE) corrections as these would likely couple to the sky brightness and/or the y-coordinate. Moreover, we performed the photometry on the images corrected for y-CTE and not surprisingly find no clear trend with y-coordinate.

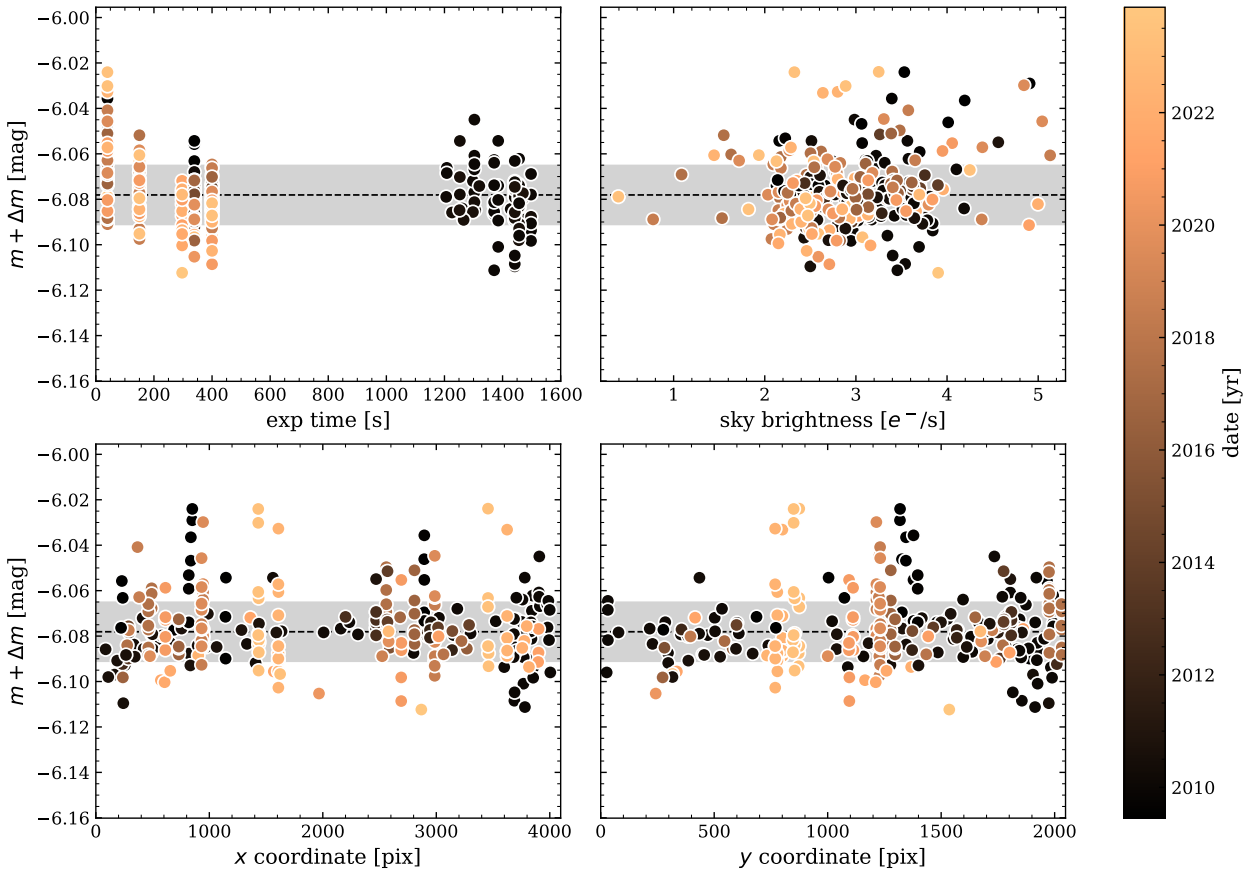

Figure 3: Residuals in photometry for star 14964. The panels show the corrected photometry as a function of exposure time (top left), sky surface brightness (top right), and x- and y-coordinate (bottom panels). The color of the symbols indicates the date of the observation as shown in the colorbar on the far right. The gray region and dotted line have the same meaning as in Figure 2. The majority of these panels show no residual trends in the continuous variables, except for the exposure time, which shows a clear offset for shortest available exposure times ($t \lesssim 200$ s). At this time we do not have an explanation for this observation, but as described in § 5 we include an additional relative calibration to address this systematic difference.

To address this systematic offset in photometry as a function of exposure time seen in Figure 3, we introduce an additional relative calibration term of the form:

$$\mathcal{E}(t) = \begin{cases} \mu\,(t - t^*) & t < t^* \\ 0 & t \geq t^* \end{cases} \tag{10}$$

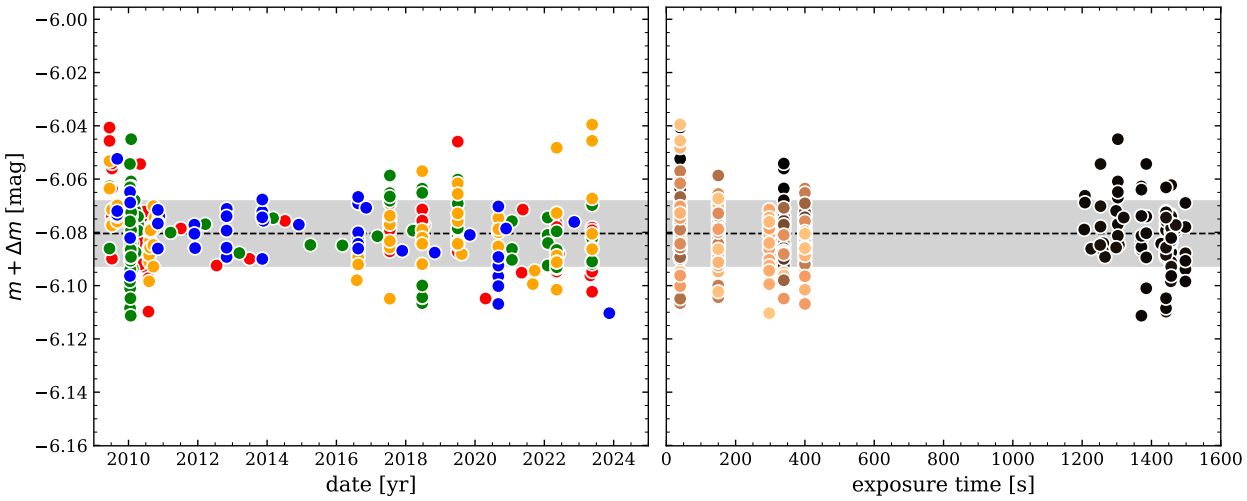

Figure 4: Updated relative calibration for star 14964. Here we only show the revised lightcurve (left panel) and the exposure-time relation (right panel), as the other parameters do not show noteworthy changes. These figures are equivalent to the right panel of Figure 2 and upper left panel of Figure 3, respectively. The gray region, dotted line, and symbol colors have the same meaning as in Figure 2 and Figure 3, though here the width of the distribution has decreased to 12 mmag as the systematic trends are further nulled out.

where μ is an additional parameter to include in $\boldsymbol{\theta}$ and determine; and we adopt $t^* = 250$ s. Our results are largely immune to the exact choice of this timescale, however it is important to require this calibration term goes to zero at some time to avoid degeneracy in the model. With this term added to the photometric model in equation (7) and finding the new optimized calibration, we show the updated lightcurve and exposure time trend in Figure 4. By construction, the correlation with exposure time is removed, without adversely affecting the lightcurve plot. Indeed, the scatter in the photometric repeatability reduces by a small amount down to $\sigma_m = 12$ mmag, which represents $\sim$6% further decrease with respect to the first model from Figure 2.

Given this model now removes all testable systematic trends, we refer to this as our "baseline" model, which has $\psi^2 = -1.00 \times 10^7$ and reduced $\chi^2/\nu = 2.29 \times 10^6/1837410 = 1.25$. In Table 1, we present the values for the explicit parameters in $\boldsymbol{\theta}$.

While our model combines all relative calibrations into a single model, it is important to compare it to previous works. In particular, we compare our derived time-dependent sensitivity for amplifier B: $\beta_B = -1.47 \pm 0.2$ mmag/yr to ≈ -0.5 mmag/yr (Bohlin, Ryon, & Anderson 2020, after transforming from their ratio of flux to a difference in magnitude as presented here). Still, the broad consistency between the measurements is reassuring, particularly when accounting for the fact that Bohlin, Ryon, & Anderson (2020) explicitly controlled for flat-fielding and amplifier/detector differences by consistently placing the standard star at the same position in all epochs. Here, we have explicitly removed those assumptions and instead included their effects (in terms of the amplitude and uncertainties in their effects). Turning to the amp-to-amp offsets (the γ-terms in equation (5)), we see that the WFC2 is $\sim$ 48 mmag offset with respect to WFC1, indicating that, for the same

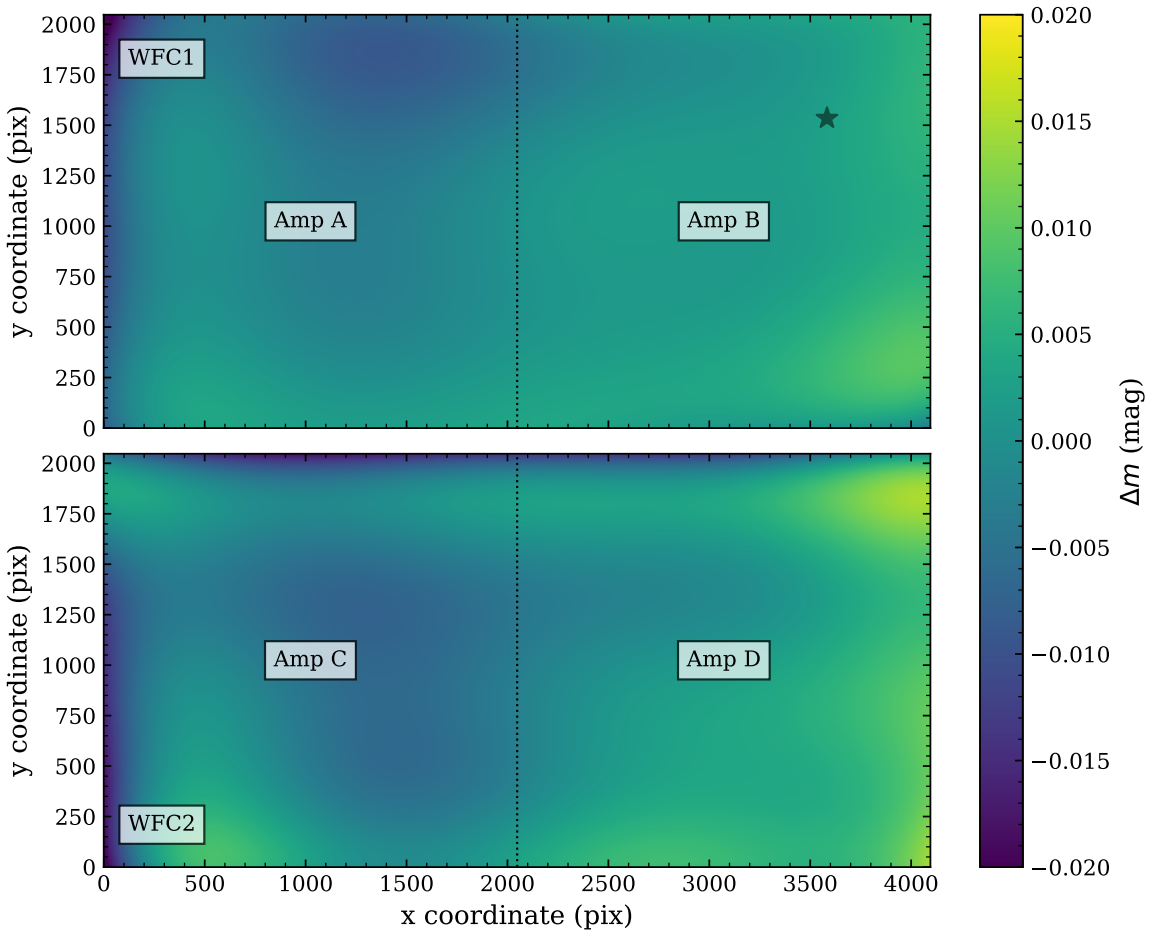

Figure 5: L-flat correction. We show the magnitude correction to apply to the flatfield file `m2f1516ej_pfl.fits`, and the multiplicative correction is just $10^{-0.4\,\Delta m}$. The star symbol at $(x, y) = (3583, 1535)$ pix is the notional position of the sensitivity monitoring from Bohlin, Ryon, & Anderson (2020).

source, it produces $\sim 4.8\%$ more photoelectrons. To reiterate, this is effectively the offset between the red/green (WFC1) and the orange/blue (WFC2) points in Figure 2.

With the baseline model that includes the exposure-time calibration, we render the two-dimensional Legendre polynomials for the two detectors to show the multiplicative correction to the flatfield file `m2f1516ej_pfl.fits` in Figure 5.

As a few final remarks on the optimization process, the computation often requires ~ 20 min to run on an Apple laptop with an M1 processor (single core) and 64 GB of RAM. However, to achieve some of this performance, we required a few code enhancements and optimizations. Specifically, to compute the corrections we use just-in-time compilation with `numba` (Lam, Pitrou, & Seibert 2015), which provides many factors of performance improvements.

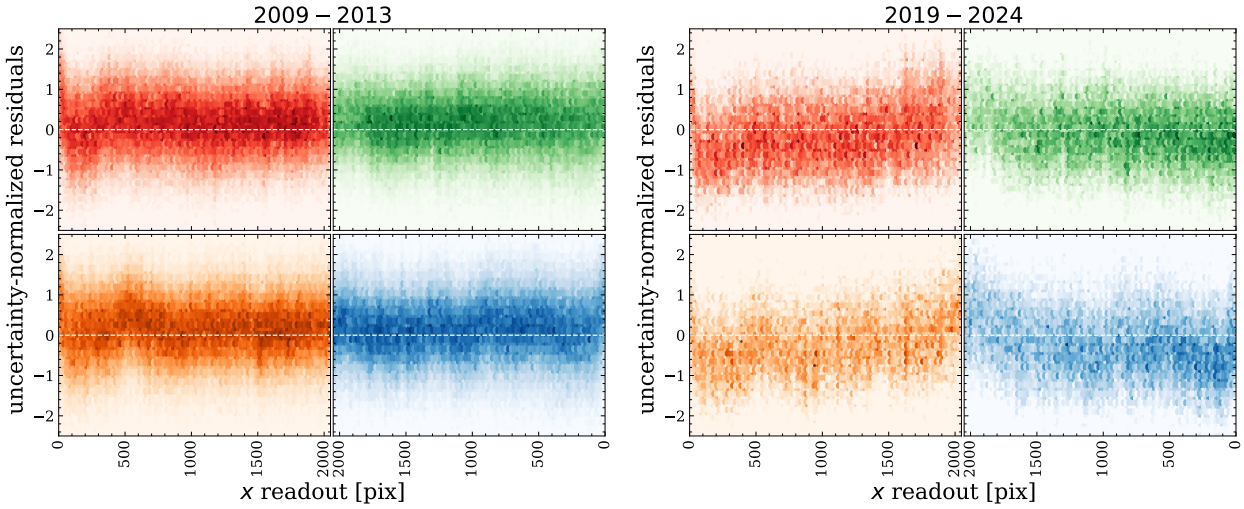

Figure 6: Losses by amplifier distance. We show the uncertainty-normalized residuals $((\hat{m} - \tilde{m})/\sigma$ — so the values can be thought of number of uncertainty deviations from the model fit) as a function of distance from the amplifier (*e.g.* x-readout) with each color referring to the four amplifiers as in Figure 2. The left set of 2×2 plots shows the data from $2009 - 2013$ while the right set shows the data from $2019 - 2024$. There is a clear trend in the late-time data where stars near the amplifier have a slightly negative residual, whereas stars far from the amplifier have positive residuals. Qualitatively speaking, this is expected behavior for serial-CTE losses, but the amplitude of the effect is not easily ascertained from this figure.

6 Conclusions and Summary

The primary strength of the Ubercal methodology is a clean separation between the relative and absolute calibrations, as it uses all data with repeated measurements of the same source(s) to constrain the former. With that in mind, the various deep fields or other cluster systems could be included in future analyses. Additionally, there are observations in F814W that would provide some color information for these calibrations. As a final remark, the reduced-χ^2 hints at additional systematic terms and one conspicuous trend concerns the serial readout correlations. In Figure 6, we show the uncertainty-normalized residuals (*e.g.* the difference between the data and the model normalized to the uncertainty) as a function of distance from the amplifier. The two sets of data show early ($2009 - 2013$) versus late ($2019 - 2024$) data, however only the early-time data show no significant trends. The late-time data shows a clear bias that the photometry of stars, where measurements far from the amplifier show positive residuals (*i.e.* lower in flux) while measurements near the amplifier show negative residuals (*i.e.* higher in flux). Importantly, the Ubercal model only corrects the photometry to the average given by equation (9), therefore this sign-flip is expected. These observations (the late- versus early-time and sign-flip), are what is qualitively expected for uncorrected serial-CTE. The Ubercal formalism is well-suited to describe the serial CTE, but would require explicitly incorporating additional parameters related to CTE (*e.g.* background, fluence, position, date, *etc.*). However calibrating the serial CTE losses is beyond the scope of this present work.

Acknowledgements — We cordially thank G. Anand, J. Anderson, M. Chiaberge, N. Grogin, and J. Mack for helpful conversations regarding CTE corrections, `hst1pass`, ACS observing, and other topics. We are additionally grateful to C. Clark, J. Ryon and D. Stark for their careful reading of this report. This work has made use of data from the European Space Agency (ESA) mission *Gaia* (`https://www.cosmos.esa.int/gaia`), processed by the *Gaia* Data Processing and Analysis Consortium (DPAC, `https://www.cosmos.esa.int/web/gaia/dpac/consortium`). Funding for the DPAC has been provided by national institutions, in particular the institutions participating in the *Gaia* Multilateral Agreement. Based on archival observations with the NASA/ESA *Hubble Space Telescope*, obtained at the Space Telescope Science Institute, which is operated by AURA, Inc., under NASA contract NAS 5-26555.

Table 1: Summary of Relative Calibration Parameters[†]

L-Flat WFC1 (mmag)	L-Flat WFC2 (mmag)	Other Parameters
$\alpha_{1,0,0} = +4.59 \pm 1.91$	$\alpha_{2,0,0} = +5.83 \pm 0.44$	$\beta_A = -1.85 \pm 0.07$ mmag/yr
$\alpha_{1,1,0} = -3.14 \pm 0.31$	$\alpha_{2,1,0} = -1.81 \pm 0.33$	$\gamma_B = -0.76 \pm 2.55$ mmag
$\alpha_{1,0,1} = +1.59 \pm 0.28$	$\alpha_{2,0,1} = +3.69 \pm 0.36$	$\beta_B = -1.47 \pm 0.13$ mmag/yr
$\alpha_{1,2,0} = +1.77 \pm 0.16$	$\alpha_{2,2,0} = +0.27 \pm 0.11$	$\gamma_C = +49.68 \pm 2.07$ mmag
$\alpha_{1,1,1} = -0.26 \pm 0.18$	$\alpha_{2,1,1} = +2.15 \pm 0.25$	$\beta_C = -2.31 \pm 0.24$ mmag/yr
$\alpha_{1,0,2} = +0.51 \pm 0.90$	$\alpha_{2,0,2} = +0.76 \pm 0.45$	$\gamma_D = +46.41 \pm 0.65$ mmag
$\alpha_{1,3,0} = +0.90 \pm 0.12$	$\alpha_{2,3,0} = +2.21 \pm 0.50$	$\beta_D = -2.05 \pm 0.11$ mmag/yr
$\alpha_{1,2,1} = +0.57 \pm 0.17$	$\alpha_{2,2,1} = -1.30 \pm 0.17$	$\mu = +0.08 \pm 0.00$ mmag/s
$\alpha_{1,1,2} = -0.33 \pm 0.14$	$\alpha_{2,1,2} = -2.02 \pm 0.13$	$\eta = -5.93 \pm 0.03$
$\alpha_{1,0,3} = -1.75 \pm 0.46$	$\alpha_{2,0,3} = -1.91 \pm 0.15$	
$\alpha_{1,4,0} = -0.93 \pm 0.47$	$\alpha_{2,4,0} = -0.91 \pm 0.51$	
$\alpha_{1,3,1} = -0.04 \pm 0.58$	$\alpha_{2,3,1} = +0.34 \pm 1.05$	
$\alpha_{1,2,2} = +2.13 \pm 0.79$	$\alpha_{2,2,2} = +0.64 \pm 0.37$	
$\alpha_{1,1,3} = +0.26 \pm 0.13$	$\alpha_{2,1,3} = -3.33 \pm 0.16$	
$\alpha_{1,0,4} = +3.90 \pm 0.91$	$\alpha_{2,0,4} = +4.83 \pm 0.34$	
$\alpha_{1,5,0} = -0.96 \pm 0.33$	$\alpha_{2,5,0} = +5.10 \pm 0.43$	
$\alpha_{1,4,1} = +0.50 \pm 0.15$	$\alpha_{2,4,1} = +0.49 \pm 0.15$	
$\alpha_{1,3,2} = +0.24 \pm 0.31$	$\alpha_{2,3,2} = +2.02 \pm 0.41$	
$\alpha_{1,2,3} = -1.12 \pm 0.77$	$\alpha_{2,2,3} = +0.56 \pm 0.44$	
$\alpha_{1,1,4} = +1.63 \pm 0.11$	$\alpha_{2,1,4} = -4.67 \pm 0.12$	
$\alpha_{1,0,5} = -2.75 \pm 0.13$	$\alpha_{2,0,5} = -2.76 \pm 0.14$	
$\alpha_{1,6,0} = +2.18 \pm 0.22$	$\alpha_{2,6,0} = -6.37 \pm 0.37$	
$\alpha_{1,5,1} = -1.30 \pm 0.32$	$\alpha_{2,5,1} = +1.53 \pm 0.23$	
$\alpha_{1,4,2} = +0.87 \pm 0.29$	$\alpha_{2,4,2} = -1.17 \pm 0.44$	
$\alpha_{1,3,3} = -3.56 \pm 0.70$	$\alpha_{2,3,3} = -0.00 \pm 0.16$	
$\alpha_{1,2,4} = +0.59 \pm 0.15$	$\alpha_{2,2,4} = -0.83 \pm 0.16$	
$\alpha_{1,1,5} = -0.03 \pm 0.12$	$\alpha_{2,1,5} = -3.31 \pm 0.14$	

[†]For the baseline model that includes exposure-time calibration.

A Program ID Numbers

The data were taken from program IDs: 11397, 11510, 11677, 11880, 11887, 12385, 12389, 12730, 12734, 13155, 13159, 13592, 13596, 13955, 13959, 14398, 14402, 14507, 14511, 14949, 14953, 15522, 15526, 15760, 15764, 16384, 16473, 16520, 16525, 16968, 16973, and 17331.

References

Anderson, J. & King, I. R., Instrument Science Report ACS 2006-01

Anderson, J. 2022, Instrument Science Report ACS 2022-04

Anderson, J. 2022, Instrument Science Report ACS 2022-02

Bellini, A., Anderson, J., & Grogin, N. A. 2018, Instrument Science Report ACS 2018-8

Bohlin, R. C., Ryon, J. E., & Anderson, J. 2020, Instrument Science Report ACS 2020-08

Borncamp, D., Kozhurina-Platais, V., & Avila, R. 2015, Instrument Science Report ACS 2015-02

Cohen, Y., Grogin, N., & Bellini, A. 2020, Instrument Science Report, 2020-01

Deustua, S., Kent, S., & Smith, J. A. 2013, in Oswalkt, T. D., Bond H. E., eds., *Planets, Stars, and Stellar Systems. Volum 2: Astronomical Techniques, Software, and Data.* Springer, Dordrecht, P. 375

Duestua, S., Rubin, D., Hounsell, R., et al. 2021, RNASS, 5, 66

Hoffmann, S. L. & Kozhurina-Platais, V. 2020, Instrument Science Report ACS 2020-09

Krist, J., 2003, Instrument Science Report ACS 2003-06

Kozhurina-Platais, V., Borncamp, D., Anderson, J., et al. 2015, Instrument Science Report ACS/WFC 2015-06

Gaia Collaboration, Prusti, T., de Bruijne, J. H. J., et al. 2016, A&A, 595, A1. doi:10.1051/0004-6361/201629272

Gaia Collaboration, Vallenari, A., Brown, A. G. A., et al. 2023, A&A, 674, A1. doi:10.1051/0004-6361/202243940

Lam, S. K., Pitrou, A. & Seibert, S., 2015. *Numba: A llvm-based python jit compiler.* In Proceedings of the Second Workshop on the LLVM Compiler Infrastructure in HPC

Mack, J., Bohlin, R., Gilliland, R., Van der Marel, R., Blakeslee, J., & De Marchi, G. 2002, Instrument Science Report ACS 2002-08

Mack, J. 2016, Instrument Science Report WFC3, 2016-05

Padmanabhan, N., et al. 2008, ApJ, 674, 1217

Úbeda, L. & Kozhurina-Platais, V. 2013, Instrument Science Report ACS 2013-03

Van der Marel, R. P. 2003, Instrument Science Report ACS, 2003-10

Virtanen, P., Gommers, R., Oliphant, T. E., et al. 2020, Nature Methods, 17, 261

Wittman, D., Ryan, R., & Thorman, P. 2012, MNRAS, 421, 2251